JACS
JOURNAL OF THE AMERICAN CHEMICAL SOCIETY
pubs.acs.org/JACS
Article

Interfacial-Assembly-Induced *In Situ* Transformation from Aligned 1D Nanowires to Quasi-2D Nanofilms

Zhen He,*,† Jie Su,† Yu-Tao Wang, Kang Wang, Jin-Long Wang, Yi Li, Rui Wang, Qing-Xia Chen, Hui-Jun Jiang,* Zhong-Huai Hou, Jian-Wei Liu,* and Shu-Hong Yu*

Cite This: *J. Am. Chem. Soc.* 2024, 146, 19998−20008

ABSTRACT: As the dimensionality of materials generally affects their characteristics, thin films composed of low-dimensional nanomaterials, such as nanowires (NWs) or nanoplates, are of great importance in modern engineering. Among various bottom-up film fabrication strategies, interfacial assembly of nanoscale building blocks holds great promise in constructing large-scale aligned thin films, leading to emergent or enhanced collective properties compared to individual building blocks. As for 1D nanostructures, the interfacial self-assembly causes the morphology orientation, effectively achieving anisotropic electrical, thermal, and optical conduction. However, issues such as defects between each nanoscale building block, crystal orientation, and homogeneity constrain the application of ordered films. The precise control of transdimensional synthesis and the formation mechanism from 1D to 2D are rarely reported. To meet this gap, we introduce an interfacial-assembly-induced interfacial synthesis strategy and successfully synthesize quasi-2D nanofilms *via* the oriented attachment of 1D NWs on the liquid interface. Theoretical sampling and simulation show that NWs on the liquid interface maintain their lowest interaction energy for the ordered crystal plane (110) orientation and then rearrange and attach to the quasi-2D nanofilm. This quasi-2D nanofilm shows enhanced electric conductivity and unique optical properties compared with its corresponding 1D geometry materials. Uncovering these growth pathways of the 1D-to-2D transition provides opportunities for future material design and synthesis at the interface.

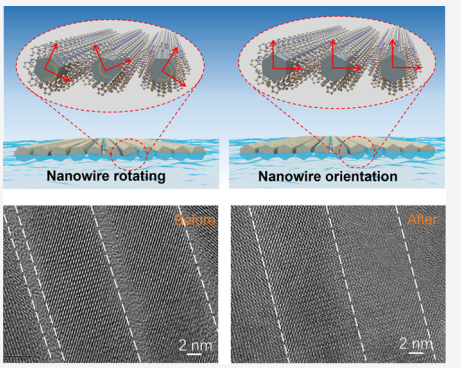

INTRODUCTION

Nanomaterials with different dimensionalities, such as one-dimensional (1D) or two-dimensional (2D) nanomaterials, exhibit differences in exposed crystal planes, morphology, size, and specific surface area, leading to their vast discrepancy of intrinsic physical and chemical properties,[1−3] which finally results in broad applications in optoelectronic devices,[4,5] catalysis,[6,7] sensors,[8,9] and many other multifunctional intelligent devices.[10−12] The 1D or 2D nanomaterials with completely the same components would always show diverse performances. For instance, the Ag nanowires (NWs) with tunable diameter exhibit better flexibility and comparable optoelectronic performance,[13,14] while the Ag nanoplates exhibit a widely tunable surface plasmon resonance (SPR) band.[15] Especially, single-chain van der Waals Te NWs encapsulated in nanotubes display a dramatically enhanced current-carrying capacity (1.5×10^8 A cm^{-2}),[16] and the single-crystalline Te NWs exhibit both chirality-dependent charge-to-spin conversion phenomena[17] and controllable inverse photoconductance.[18] As a comparison, the 2D tellurium (tellurene) would like to show chirality-dependent properties, such as opposite spin textures, current-induced spin polarization, and circular photon drag effect.[19−21] These differences might be attributed to the low-dimensional confinement with different symmetry. Therefore, optimizing material growth techniques to precisely control transdimensional transitions have been a challenging task, while the experimental advances and the underlying mechanism for such transitions have been scarce so far.

Typically, manufacturing nanomaterials from lower to higher dimension must break through the energetically stable state.[22] For instance, the zero-dimensional (0D) CdTe nanoparticles were reorganized into 1D NWs *via* the removal of protective and stabilized surfactant,[23] and the 0D Ag clusters were transformed into single-cluster nanowires *via* polyoxometalate-assisted coassembly.[24] The transition from 0D perovskite quantum dots to 1D NWs[25] and eventually growth into 2D perovskite nanosheets[26] would basically require a high-temperature solvothermal condition to activate the surface atoms. The cobalt oxide nanoparticles transform into 2D nanosheets predominantly driven by negative surface energy.[27] Obviously, the surfactant acting as stabilizers can reduce the surface energy of nanomaterials, but further impedes their

Received: March 15, 2024
Revised: May 19, 2024
Accepted: May 20, 2024
Published: June 12, 2024

transdimensional growth. Furthermore, in addition to the solvothermal strategies, interfacial synthesis has become well-known for directing the assembly of precursors or the nucleation and growth of intermediates at a confined interface, showing advantages in fabricating monolayer nanofilms.[28−31] In particular, pioneered by Yang and co-workers, the liquid−air interface, typically including the Langmuir−Blodgett (LB) method, has been utilized to assemble individual inorganic nanostructures, such as nanowires,[32,33] nanorods,[34] and nanoparticles,[35,36] into ordered monolayer nanofilms. For instance, a centimeter-scale copper-based metal−organic framework film with precisely oriented structure was fabricated *via* a semiautomatic liquid−air method.[37] A chiral CdSe/CdS nanorod film was prepared by controlling the rotation angle between different layers.[38] In recent years, precise control of the transformation from 0D nanostructures to ordered 2D planar arrays and 3D supercrystals with intricate architectures has been experimentally verified,[39] while nanoparticle-based superstructure phase diagrams have been established for providing well prediction under various solvent evaporation conditions.[37,40] Despite these successful preparation methods of nanofilms, less researches have concerned on the crystal plane orientation of nanowires because the lack of crystal plane information and the high aspect ratio induced difficulties in assembly, while achieving the precise control over interfacial synthesis and identifying the driving force for dominating the nanowire oriented attachment remains challenging.[33,41]

Herein we report an *in situ* interfacial-assembly-induced interfacial synthesis (IAIS) strategy for the controlled preparation of a centimeter-scale quasi-2D nanofilm by using a well-aligned 1D NW film as a precursor, which shows an ordered crystal plane due to the oriented attachment process. Ensemble-averaged energy sampling of 1D NWs on the liquid−air interface reveals the lowest interaction energy in configurations of ordered crystal orientation. Our experiment and synchrotron-based small-angle X-ray scattering (SAXS) results indicate that NWs prefer to gradually attach and be constrained to the quasi-2D nanofilm with good crystallinity. The molecular dynamics and Monte Carlo simulations were used to elucidate the oriented attachment process and the driving force for the 1D-to-2D transformation.

EXPERIMENTAL SECTION

All chemicals were commercially available from Sinopharm Chemical Reagent Co., Ltd. and used in this experiment without further purification.

Synthesis of Te NWs. Te NWs were synthesized *via* a modified hydrothermal process, as reported previously.[42] In detail, 4 mmol of Na_2TeO_3 and 2.5 g of polyvinylpyrrolidone (PVP) were added to 64.5 mL of deionized water to form a homogeneous solution. Subsequently, 8 mL of ammonium hydroxide and 4 mL of hydrazine hydrate were added, and the mixture was stirred for 30 min. After mixing homogeneously, the solution was transferred into the autoclave reactor and kept at 180 °C for 6 h. With natural cooling at room temperature, the obtained Te NW raw solution was stored at 4 °C before use. In a similar process, Te NWs with tunable diameter could be obtained by adjusting the dosage of hydrazine hydrate. As characterized, nanowires with two different sizes (19.5 ± 1.1 and 12.2 ± 0.7 nm) were applied the followed experiment (Supplementary Figure 1).

Interfacial Synthesis of the Quasi-2D Te Nanofilm. The quasi-2D-Te film was obtained *via* an interfacial synthesis process. First, 1 mL of Te NW raw solution was precipitated by 3 mL of acetone and then dispersed in 1 mL of DMF to form a homogeneous solution. Then an equal volume of chloroform (1 mL) was added to the mixed solution and shaken evenly. The formed solution was dropped onto the water surface at the trough of an LB machine (Finland Kibron, G2-LB) *via* a 100 μL microsyringe and a total volume of 500 μL. After waiting 10 min for the evaporation of solvent, the nanowire film floating on the water surface was compressed at a speed of 0.06 mm/min (at both barrier side), which finally afforded an aligned monolayer NW film at 70 min. Subsequently, the formed NW film was transferred onto the glycol surface and moved to an oven. The oriented attachment process was performed at 180 °C for X h (X = 4, 6, 8, 10, 12) under a vacuum environment. After heating, the quasi-2D Te film was obtained and could be transferred to any substrates for further characterization.

Fabrication of Electronic Devices. Te NW monolayers and quasi-2D Te film were transferred onto precleaned Si/SiO_2 (SiO_2 layer with a thickness of 100 nm) substrates, respectively. The electrode pattern was created in the Micro and Nanoscale Research and Fabrication Lab at our university. After coating with a layer of AZ 6112 photoresist film with a thickness of 1 μm, a precision photomask was used to obtain the designed pattern *via* standard UV photolithography coupled with electron-beam evaporation. Hundreds of patterned electrodes were fabricated on a large-scale film. The testing process was performed in a probe station to electrically connect with Au electrodes, and the data were recorded by a Keithley 4200-SCS testing system.

Sample Characterizations. XRD analyses were carried out with a Rigaku DMax-gA rotation anode X-ray diffractometer equipped with graphite-monochromatized Cu Kα radiation (λ = 1.54178 Å). Transmission electron microscopy (TEM) images were obtained from a Hitachi H7650 transmission electron microscope with a CCD imaging system at an acceleration voltage of 100 kV. High-resolution TEM (HRTEM), scanning TEM (STEM) images, and *in situ* movies were performed on a JEOL ARM-200F transmission electron microscope at an acceleration voltage of 200 kV. Selected-area electron diffraction (SAED) was carried out with the ARM-200F microscope. The Raman spectra were carried out with a Renishaw inVia Reflex Raman spectrometer with an edge filter cutoff of 112 cm^{-1}. The laser excitation wavelength was 632.8 nm. A linear polarizer was placed in front of the spectrometer to polarize the reflected light in the same direction as the incident light. By rotating the nanofilm, an angle-resolved Raman spectrum can be obtained. The electrical resistance of the devices was measured through the $I-V$ testing program *via* the Keithley 4200 SCS testing system.

Ensemble-Averaged Interaction Energy Sampling of 1D Nanowires on the Liquid−Air Interface. In order to investigate how the ordered crystal orientation emerges on the liquid−air interface, we sampled the ensemble-averaged interaction energy as a function of the NW orientation ordering as follows.

To quantitatively describe the orientation ordering of NWs, we define the orientation of the ith NW, ϕ_i, as the angle between the positive X axis (which is parallel to the liquid−air interface) and the normal vector of the (100) facet closest to the positive X axis, as shown in Figure 1b. ϕ_i is positive if the normal vector is in the first quadrant and negative if it is in the fourth quadrant, so that $\phi_i \in [-\pi/6, \pi/6]$. For an ordered NW configuration with face-to-face arrangement, all of the ϕ_i are 0, while for a disordered arrangement the ϕ_i are randomly distributed in $[-\pi/6, \pi/6)$. Thus, we introduce an order parameter Q to measure the orientation ordering as $Q = 1 - \phi_{max}/(\pi/6)$, where ϕ_{max} is the maximum value that $|\phi_i|$ can reach (Figure 1b). As Q increases from 0 to 1, the orientation of NWs changes from disordered to ordered (Figure 1b).

The attractive interaction between the crystal plane of NWs can be described similarly to the form of Debye−Hückel electrostatic screening,[43] and hence, this interaction between the ith and jth NWs can be written as

$$U_{att}(\Delta r_{ij}, \phi_i, \phi_j) = -\frac{C \exp[-\lambda(r_{ij} - 2a)]}{\Delta r_{ij}^{\,2}}\left[\frac{1}{2}\cos(6\phi_i) + 1\right]\left[\frac{1}{2}\cos(6\phi_j) + 1\right]$$

https://doi.org/10.1021/jacs.4c03730
J. Am. Chem. Soc. 2024, 146, 19998−20008

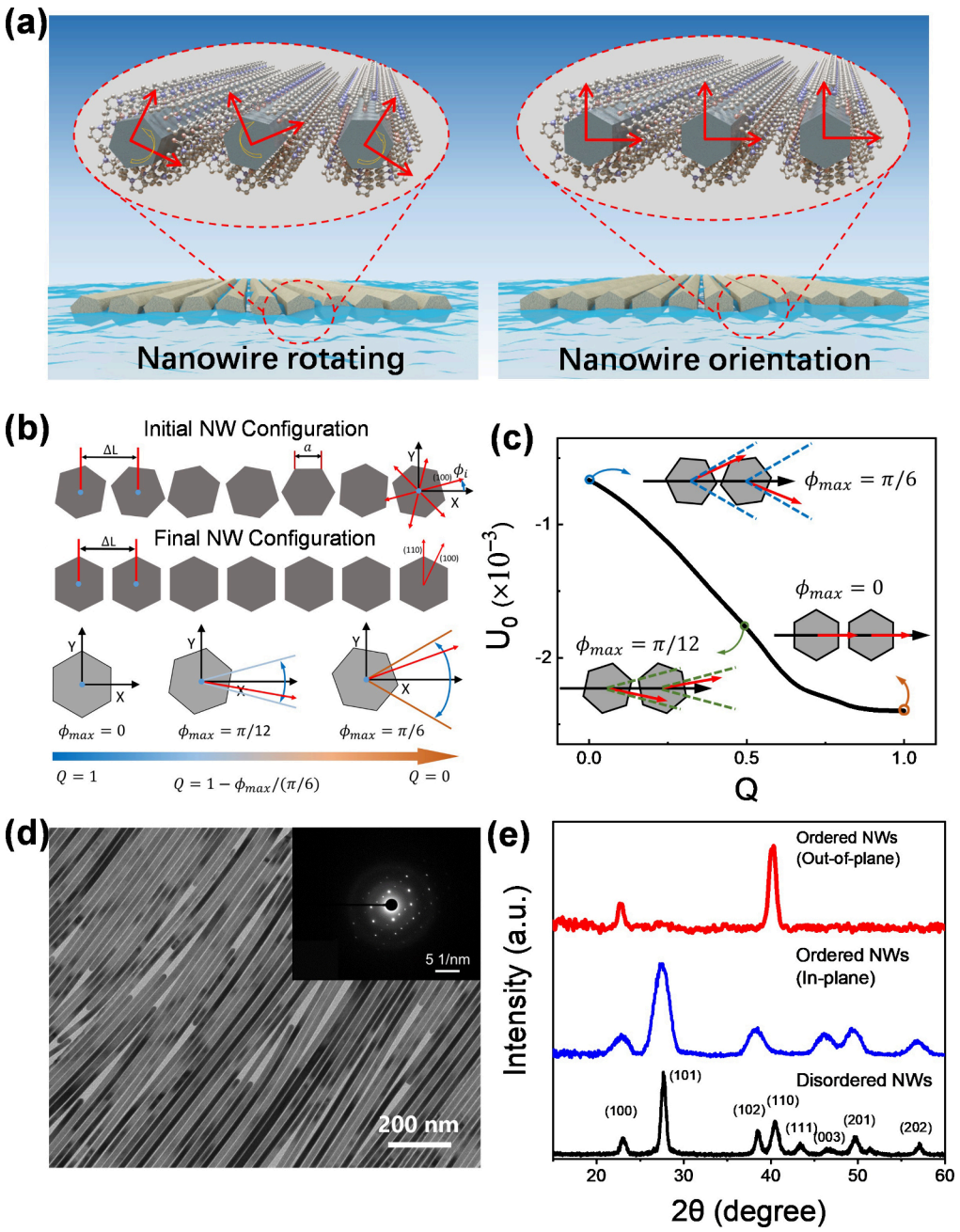

Figure 1. (a) Schematic illustration of Te NWs floating on the water surface, rotating from a disordered crystal plane to an ordered one. (b) Schematic illustration of NWs showing random orientation for $Q = 0.5$ and ordered crystal plane for $Q = 1$, respectively. These NWs are arranged with a fixed distance ΔL between two neighbors. The orientation ϕ_i is shown in the rightmost one. The definition of the order parameter Q which can characterize the orientation ordering is given at the bottom, in which ϕ_{max} is the maximum value that $|\phi_i|$ can reach. (c) Dependence of the ensemble-averaged interaction energy U_0 on the order parameter Q. The insets are typical snapshots of two NWs as examples at $Q = 0$, 0.5, and 1, respectively. (d) TEM image of NW film with ordered crystal plane. The inset shows the corresponding SAED image. (e) XRD patterns of Te NW films with ordered (out-of-plane, in-plane) and disordered structures.

where C is the interaction strength, λ^{-1} is the corresponding screen length, a is the side length of NWs, and Δr_{ij} is the distance between the centers of the ith and jth NWs. Herein, the first factor rapidly decreases as Δr_{ij} increases. The last two factors represent the influence on the attractive interaction by the orientation of NWs. Note that the repulsive interaction between NWs is caused by the volume exclusion of the soft surfactant attached to the NW surface, which is almost unchanged with different ϕ_i. Thus, for a configuration of N_0 NWs, the total interaction U_0 of the system then can be written as

$$U_0 = \sum_{i=1}^{N_0} \sum_{j=1, j\neq i}^{N_0} U_{att}(\Delta r_{ij}, \phi_i, \phi_j)$$

In the experimentally obtained assembly, the gaps between 1D NWs are nearly equal and fixed. Thus, we consider NWs separated with a fixed distance ΔL between adjacent ones so that $\Delta r_{ij} = |i - j|\Delta L$. During sampling, we fix $N_0 = 10$, $C = 10^{-4}$, and $\lambda = 1$. Based on the experimental data, it is known that the average diameter of NWs is 19.5 ± 1.1 nm and the average NW separation distance is 21.5 nm. Therefore, we fix $2a = 1$ and $\Delta L = 1.1$. For each value of Q, we calculate U_0 for an ensemble of 10^6 samples with ϕ_i randomly

https://doi.org/10.1021/jacs.4c03730
J. Am. Chem. Soc. 2024, 146, 19998−20008

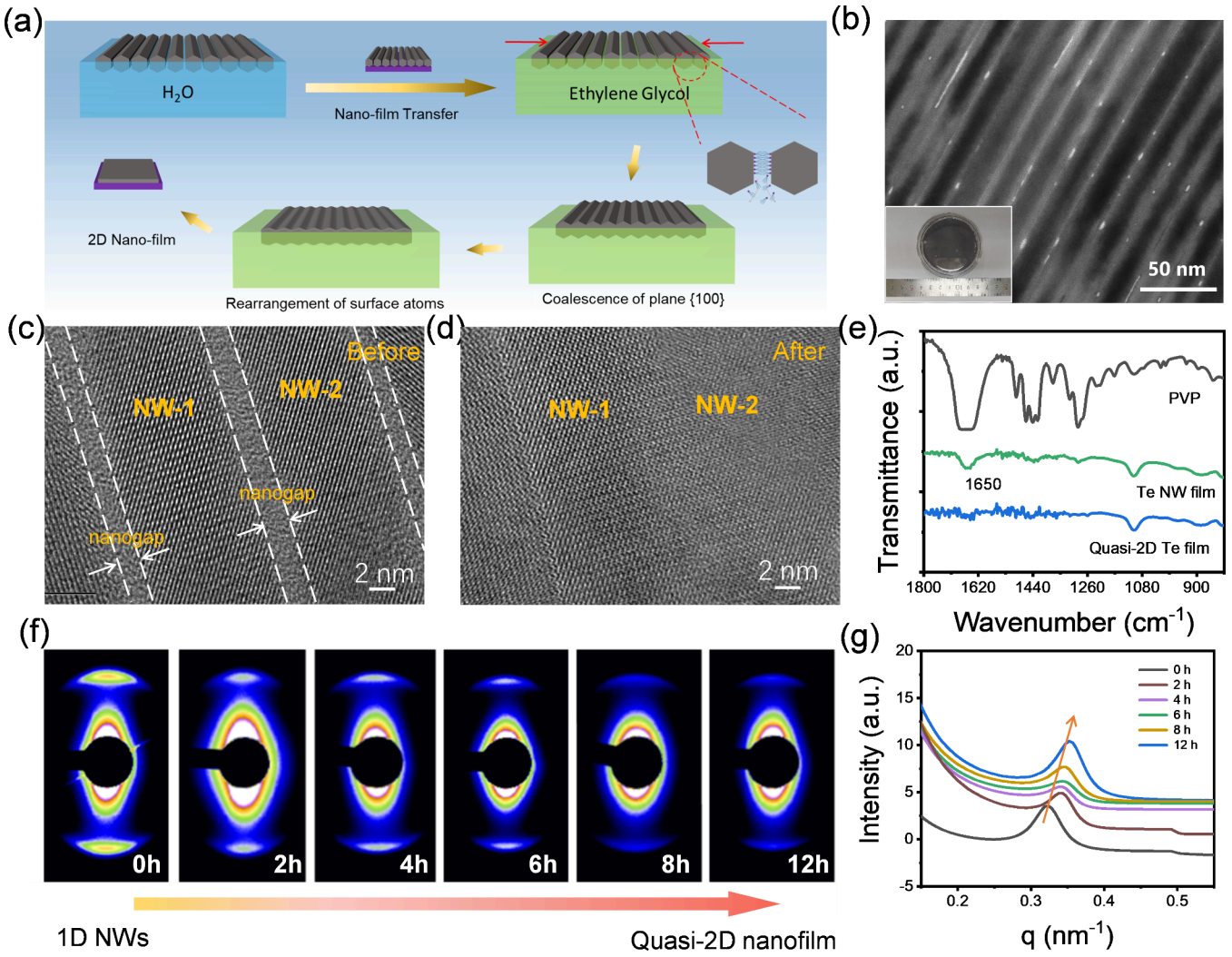

Figure 2. Oriented attachment process of aligned Te NW film to quasi-2D Te nanofilm. (a) Schematic illustration of the oriented attachment process in which aligned NWs are transformed into a quasi-2D Te nanofilm. (b) TEM image of the obtained quasi-2D Te nanofilm. The inset shows a photo of a quasi-2D Te nanofilm with a diameter of 6 cm. (c, d) HRTEM images of aligned Te NWs and quasi-2D Te nanofilm (reaction at 180 °C for 12 h), respectively. The white dashed lines represent the boundaries of nanowires, and the yellow labels mark NW-1, NW-2, and nanogaps. (e) Fourier transform infrared (FT-IR) spectra of pure PVP, Te NW film, and quasi-2D Te nanofilm. (f) 2D SAXS scattering patterns of the nanofilm formed at different reaction times to reveal the structure evolution. (g) In-plane SAXS diffraction patterns at various reaction times.

distributed in $[-\phi_{max}, \phi_{max})$. The obtained U_0 dependent on Q is presented in Figure 1b.

RESULTS AND DISCUSSION

Formation of the Monolayer Te NW Film with Ordered Crystal Orientation. As the research model, Te NWs were first synthesized *via* a hydrothermal process and assembled into an ordered NW film at the liquid−air interface, as reported previously.[44] Due to their anisotropic chiral crystal structure, the morphology of Te NWs was approximately hexagonal but not perfect cylinder.[45] The alignment of Te NWs also shows ordering in the crystal structure. As illustrated in Figure 1a, the aligned Te NWs were first formed on the liquid−air interface with random crystal orientation and then rotated to NWs with ordered orientation with the same crystal direction.

To elucidate the transformation process on the liquid−air interface, ensemble-averaged interaction energy sampling of the aligned 1D NWs with different orientations ϕ_i was performed (Figure 1b). Here we introduced an order parameter Q to measure the NW orientation ordering as $Q = 1 - \phi_{max}/(\pi/6)$ where ϕ_{max} is the maximum value that $|\phi_i|$ can reach (details can be found in the Experimental Section). Therefore, NWs with random crystal plane distribution resulted in $Q = 0$, while NWs with face-to-face ordered arrangement led to $Q = 1$ (Figure 1b). Figure 1c shows the dependence of the ensemble-averaged interaction energy U_0 on the order parameter Q. The calculated results reveal that U_0 decreases monotonically as Q increases, indicating that U_0 arrives at its minimum when Q is equal to 1, *i.e.*, the system reaches the steady state when the configuration of adjacent NWs is perfectly face-to-face. In other words, individual NWs will rotate on the interface to adjust their crystal orientation to reduce the interaction energy of the assembly structure (Figure 1d). According to the selected-area electron diffraction (SAED) pattern in the final assembly stages, the NW film with ordered crystal plane shows distinct diffraction points (inset of Figure 1d), while the NW film with a disordered crystal plane shows diffraction rings (Supplementary Figure 2). Furthermore, as shown in Figure 1e, the X-ray diffraction

https://doi.org/10.1021/jacs.4c03730
J. Am. Chem. Soc. 2024, 146, 19998−20008

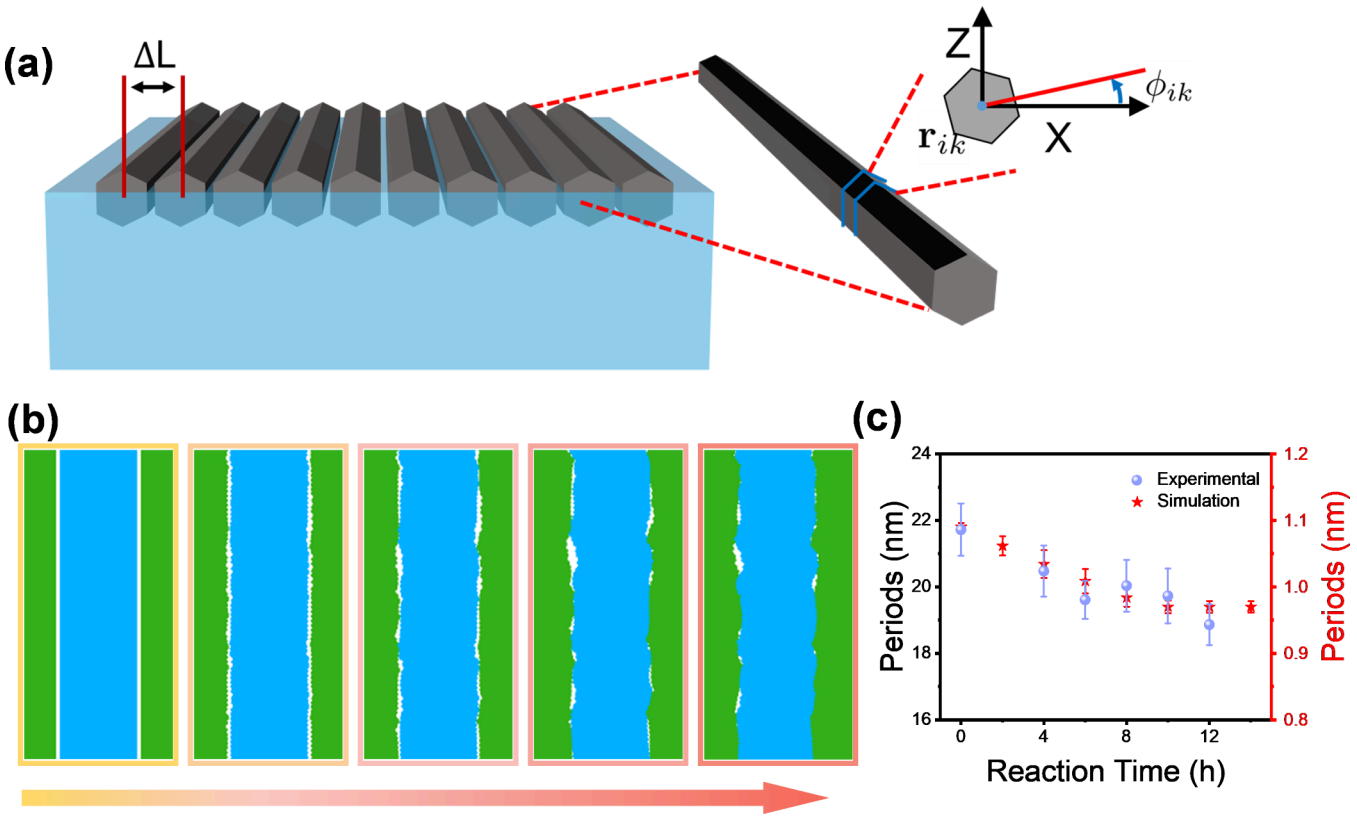

Figure 3. (a) Schematic of the system: Te NWs lie on the liquid−air interface and are arranged with the separation distance ΔL due to the adsorbed surfactant. Each NW is considered a rigid chain consisting of many hexagonal units, as presented by the blue lines. The right side picture is the cross-section of a unit with a center of mass located at r_{ik} and the orientation ϕ_{ik}. (b) Typical snapshots at t = 0, 5, 15, 25, and 35, respectively. Herein, the unit of time is 0.4 h. For clarity, all these snapshots are zoomed in so that only three NWs can be observed, and neighboring NWs are filled in different colors (blue or green). (c) Dependence of the average separation distance $\Delta\bar{L}$ on the evolution time t.

(XRD) pattern of the ordered NW film (out-of-plane) with highly ordered crystal plane shows two distinguished peaks for (100) and (110), while that of NW film with disordered crystal plane exhibits more peaks, which confirmed that the (110) plane is verticle to the substrate. Besides, the (101) (and also (202)), (102), and (003) peaks are detected in the in-plane XRD spectrum, while the (110) peak disappeared, which confirmed the attachment between (100) planes. Moreover, as shown in Supplementary Figure 3, the intensity profile of the (101) lattice parameter with respect to the azimuthal angle of the incident radiation shows the four maxima observed at 31°, 145°, 211°, and 325°. The adjacent angle is 114° and 66°, respectively, which is consistent with the included angle between the (101) and $(\bar{1}01)$ planes and between the (101) and $(10\bar{1})$ planes of the Te nanowire crystal structure. In addition, the intensity profile of the (001) lattice parameter concerning the azimuthal angle of the incident radiation shows the two maxima at 90° and 270°, confirming the anisotropic structure of the Te nanowire crystal. Furthermore, the scanning transmission electron microscopy (STEM) image in Supplementary Figure 4 also confirmed the crystal orientation of ordered nanowires and that the cross-section of the crystal exhibited the face-to-face aligned structure. Therefore, these diffraction patterns verified the orientation process of NW crystal planes at this special assembly stage.

Formation of the Quasi-2D Te Nanofilm via Interfacial Attachment Process. The obtained ordered NW film, with the same crystal plane orientation, shows surfactant attached to the NW surface and forms inevitable gaps between NWs. To investigate the transformation from 1D NWs to the 2D nanofilm, we performed an *in situ* IAIS strategy on the liquid−air interface and explored their dynamic attachment process (Figure 2a). In detail, the obtained aligned NW film was transferred onto the surface of ethylene glycol because of its high boiling point and good solubility of the surfactant. Then with the increased temperature of the environment, detachment of the surfactant facilitates the oriented attachment of NWs, resulting in the formation of the macroscale quasi-2D nanofilm. The obtained quasi-2D nanofilm shows a compact nanostructure as the boundaries of NWs are connected together (Figure 2b). As a comparison, before the *in situ* heating process, aligned NWs show an apparent gap of 2 nm between the adjacent NW-1 and NW-2 (Figure 2c; the white dashed lines represent the boundaries of nanowires). After 12 h of reaction, NW-1 and NW-2 were bound together to form the quasi-2D nanofilm with connected boundary but no gap (Figure 2d). According to scanning electron microscopy (SEM) images at different locations of the nanofilm (Supplementary Figure 5), the film exhibits the same orientation but with only several pores or cracks, demonstrating its homogeneity. Typically, the subphase solvent of ethylene glycol with raised temperature accelerates the dissolution of surfactant on the NW surface, which promotes the collision and attachment of NWs on the (100) facets. The IR result reveals the characteristic stretching vibration peak of the carbonyl group in the Te NW film (1650 cm^{-1}). As a comparison, that peak disappeared in the quasi-2D Te nanofilm (Figure 2e), proving the detachment of

https://doi.org/10.1021/jacs.4c03730
J. Am. Chem. Soc. 2024, 146, 19998−20008

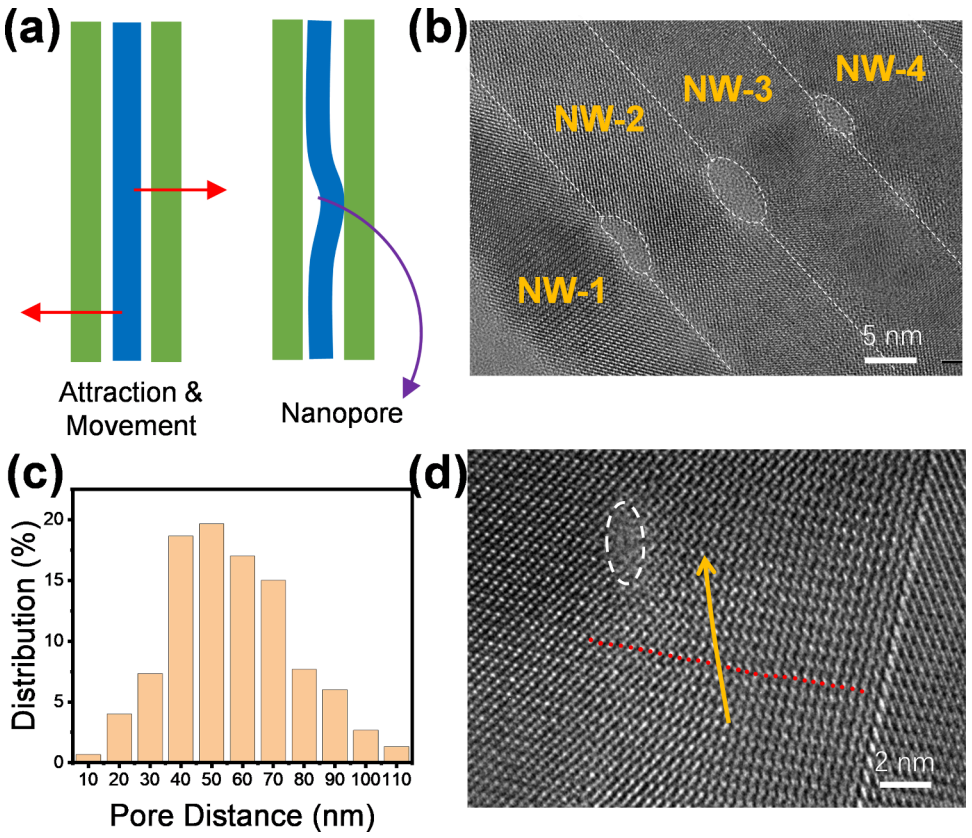

Figure 4. (a) Schematic illustration of the formation of a nanopore. (b) TEM image of the obtained quasi-2D Te nanofilm, showing nanopores at the boundaries. The white dashed lines represent the previous boundaries of NWs, and the white circles mark the nanopores. (c) Statistical distribution of the distance between two adjacent nanopores along the length direction. (d) HRTEM image of the nanopore and the nearby contorted crystal structure. The red dots exhibit the bending of the crystal structure. The yellow arrow marks the bending direction.

surfactant.[46] More importantly, the period of the NW film gradually decreased as the interfacial synthesis proceeded. Therefore, we adopted small-angle X-ray scattering (SAXS) characterization in the BL16B beamline of the Shanghai Synchrotron Radiation Facility to address the NW film structure evolution. The 2D scattering patterns show an isotropic scattering ellipse shape with two symmetry peaks, representing the highly ordered NW structure (Figure 2f). With increased interfacial synthesis time, the corresponding symmetry scattering peaks weakened, indicating the decrease in the long-range order of the NW anisotropic structure, which might be attributed to the effect of gradually increased connection dots between ordered NWs. According to the in-plane SAXS diffraction patterns (Figure 2g), the scattering signals along the ordered direction showed a peak at q = 0.32 nm^{-1} that gradually increased to q = 0.35 nm^{-1}, which demonstrated a 9% decrease in the NW ordering period.

To further investigate the formation mechanism of the quasi-2D nanofilm from the assembled 1D NWs, we performed a molecular dynamics simulation of the NW attachment process. Firstly, we ran the dynamics simulation in a quasi-2D box consisting of 40 Te NWs separated with a fixed distance ΔL between adjacent ones (Figure 3a) to be the initial state. Each NW is discretized as a rigid chain consisting of N hexagonal segments with the side length a and thickness d. In the initial state, the repulsive interaction caused by the volume repulsive interaction of surfactant adsorbed on the NW surface is in balance with the attractive interaction between the crystal plane of NWs. When NWs were transferred onto the surface of ethylene glycol under an elevated temperature, the surfactant preferred to dissolve in ethylene glycol rather than stay at the liquid-gas interface or attach on the surface of NWs, leading to shorter and shorter equilibrium distances between NWs with increasing time (details can be found in the Supplementary Methods 1). According to the simulation results, the dynamic attachment movie and typical snapshots are shown in Video S1 and Figure 3b, respectively. For clarity, all these snapshots are zoomed in with only three NWs. It can be seen that all NWs are arranged in parallel with the same separation distance in the initial time. As time increases, NWs become closer and closer due to the repulsive interaction is weaker than the attractive one. In addition, with the increased temperature, the Brownian movement would certainly be accelerated because of the thermal noise, leading to the shaking and colliding of NWs with each other. As the reaction time prolongs, the collision points of NW pieces coalesce together and gradually expand, much like the zipper closing process. Finally, NWs aggregate together to form a nanofilm with many nanopores. In order to quantitatively characterize this attachment process, the time dependence of the average separation distance of two adjacent NWs, $\Delta\bar{L}$, is plotted in Figure 3c. It is observed that $\Delta\bar{L}$ decreases with increasing time first and finally remains constant, representing that the system reaches a steady state, which aligns with the observed experimental result (Supplementary Figure 6). To summarize, the origin of this attachment process of NWs results from the imbalance between the attractive interaction of NWs and the repulsive interaction of NWs caused by the attached surfactant.

https://doi.org/10.1021/jacs.4c03730
J. Am. Chem. Soc. 2024, 146, 19998−20008

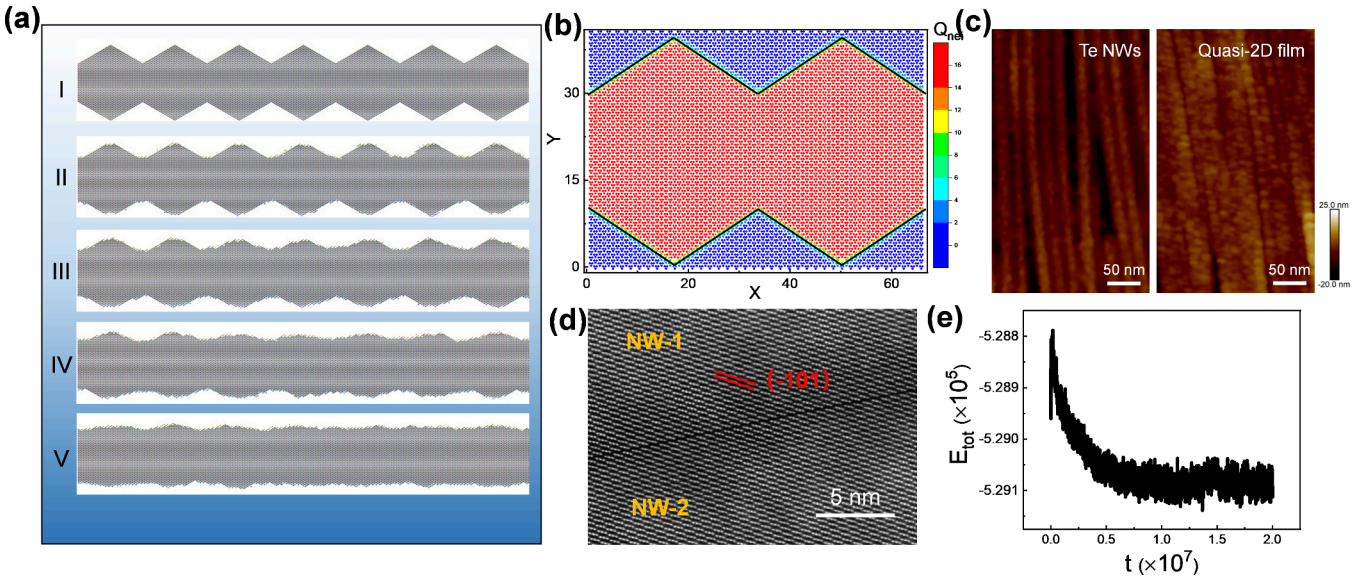

Figure 5. (a) Typical snapshots at the MC steps t = 0, 10^6, 2×10^6, 5×10^6, and 2×10^7, respectively. (b) The energy caused by adjacent atoms for all sites. The black lines are the boundaries of nanowires in the initial state. (c) Height mapping of aligned Te NWs and quasi-2D Te nanofilm. (d) STEM image of the attachment interface of the quasi-2D Te nanofilm. The yellow labels mark NW-1 and NW-2. (e) Dependence of the total energy of the system E_{tot} on the evolution MC step t.

When NWs are transferred onto the surface of ethylene glycol under an elevated temperature, surfactant prefers to detach from the surface of NWs and dissolve in the solvent, leading to a weaker repulsive interaction than the attractive one.

During the oriented attachment process, both the experiment and simulation results confirm the existence of defects on the 2D nanofilm. As an example presented in Figure 4a, the bottom and top of the NW (marked as blue) are closer to its left neighbor (marked as green), while the middle part is closer to its right one, caused by thermal noise.[47,48] Because the attractive interaction of NWs gets more robust with the decreasing separation distance, the bottom and the top of the blue NW would attach on its left neighbor while the middle part would attach on its right one, forming three attachment points and further leading to a nanopore. Due to the high aspect ratio, plenty of attachment points on the NW boundary will simultaneously form, which inevitably produces many nanopores and causes stress between NWs. As a result, the nanopores with different elliptical morphologies can be confirmed (Figure 4b). By statistical calculation, 70% of the pore distances in the length direction are concentrated in the range of 40−70 nm (Figure 4c and Supplementary Figure 7). Therefore, the attachment of adjacent NWs and the evolution of these defects is vital to the transformation process. Significantly, most of the nanopores show different shapes, such as the ellipse forms and the strip forms (Supplementary Figure 8), and the crystal structure near the pores has some conspicuous tortuosity (Figure 4d), further confirming that the bending of NWs induced by thermal noise is responsible for the formation of nanopores.

Morphology Changes of Te NW in Cross Section at the Atomic Scale. Once NWs collide to attach together, the lower amount of surfactant on the NW surface led to an unstable state of the nanofilm. The potential energy difference of Te atoms on the top of NWs would result in an unstable disturbance, which might cause the rearrangement of surface atoms for the minimum energy of the nanofilm. In order to elucidate the rearrangement dynamics at the atomic scale, we employed Monte Carlo (MC) simulations (Supplementary Methods 2) to investigate how the morphologies of NWs and nanopores change. As shown in Supplementary Figure 9, according to the special hcp crystal structure of Te NWs, we adopt a configuration (with periodic boundary conditions) consisting of three layers of Te atoms as an example. Thus, individual Te atoms (shown as red balls in Supplementary Figure 10) have three types of adjacent atoms, and the system's total energy (E_{tot}) is concerned with the moving atom's position. As shown in Figure 5a, 10 perfectly lapped NWs attached without any gaps are defined as an ideal initial configuration. Each side of the NW includes 20 atoms (corresponding to an NW with a diameter of around 20 nm), and consequently, the total number of atoms in the configuration is 33630. As reaction time increases, the Te atoms move from the sites on the convex boundary to sites on the concave so that the hexagonal NWs become more and more flattened (Supplementary Video 2). In detail, the energy caused by adjacent atoms for all sites in the initial state is presented in Figure 5b. As the energy of occupied sites inside NWs is lower than that on the boundary, Te atoms prefer a configuration with a smaller surface-to-volume ratio to obtain lower total energy. Therefore, Te atoms will move from the sites on the convex boundary to the concave boundary, eventually leading to a flattened nanofilm (Supplementary Methods 2). The height mapping of the AFM image confirmed the surface fluctuation of the quasi-2D nanofilm (Figure 5c and Supplementary Figure 11), which is in accordance with the simulation results. The STEM image of the boundary confirmed the well-attached edge of Te NWs (Figure 5d). Besides, the dependence of the system's total energy on the evolution MC step reveals that after passing a barrier, the energy decreases to a constant with fluctuations, indicating the steady state of nanofilm (Figure 5e).

Furthermore, we also consider the initial configurations of lapped NWs with nanopores of three different sizes. As respectively presented in Supplementary Figure 12, all nanopores change from large to small (Supplementary Videos

https://doi.org/10.1021/jacs.4c03730
J. Am. Chem. Soc. 2024, 146, 19998−20008

3, 4, and 5). The underlying mechanism is similar to that mentioned above: Te atoms prefer to move from the sites on the convex boundary to sites on the concave boundary, including the nanopore, to obtain a smaller surface-to-volume ratio. Finally, the smallest nanopore is filled with Te atoms (Supplementary Figure 12g), while the other two larger ones still exist but become much smaller (Supplementary Figure 12h,i). The total energy of each system shows a similar decreasing tendency and finally maintains constants with fluctuations (Supplementary Figure 12j–l), indicating that systems with smaller and even disappearing nanopores reach a steady state.

Anisotropic Properties of the Quasi-2D Nanofilm. The transformation of Te from an aligned NW monolayer to a quasi-2D nanofilm can also affect their intrinsic properties. We characterized the optical properties of the quasi-2D nanofilm by polarized Raman spectroscopy at room temperature. As shown in Figure 6a, the Raman spectrum shows three peaks at

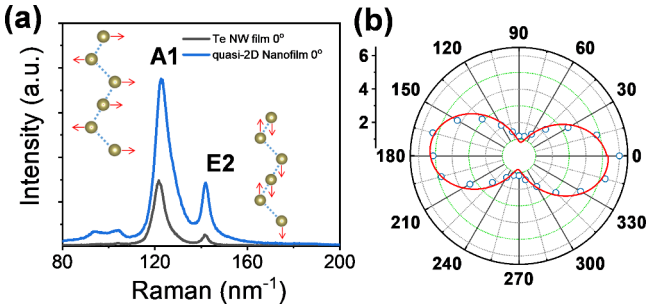

Figure 6. (a) Raman spectra for 1D Te NW film and quasi-2D Te nanofilm with 0° degree polarization that parallel to the nanowire orientation. (b) Angle-resolved Raman spectra for quasi-2D Te nanofilm with A_1 mode located at 122 cm^{-1}.

92, 122, and 143 cm^{-1} corresponding to the E_1, A_1, and E_2 modes, which is in agreement with the previous reports.[49] The A_1 mode represents the chain expansion mode, in which each atom moves in the basal plane (100), while the additional two degenerate E_1 and E_2 modes can be attributed to bond bending along the *a* axis and bond stretching along the *c* axis (001), respectively (Supplementary Figure 13).

As shown in Figure 6, the assembled structure of Te NWs shows a low-anisotropy absorption of the A_1 mode in the Raman spectra. During the transformation process, the A_1 mode gradually shifts from 121.5 cm^{-1} to the high-wavenumber side (122.7 cm^{-1}) for the quasi-2D nanofilm in the parallel direction, revealing that the atom structure changes in the basal plane (100) (Figure 6a). Besides, the E_1 mode in the quasi-2D nanofilm splits into a doublet at 93.4 and 103.8 cm^{-1} for transverse (TO) and longitudinal (LO) phonons, respectively, similar to previously reported bulk or nanostructured tellurium.[50,51] As the period and thickness decrease, the deformation potential in the quasi-2D nanofilm lattice increases while the electro-optic effect weakens, leading to the appearance of the E_1(LO) mode in the Raman spectrum for quasi-2D Te crystals. We extracted the peak intensities of the A_1 mode by fitting with a Lorentz function and plotted them in a polar curve (Figure 6b). It is worth noting that the A_1 plot shows a minimum intensity and a maximum intensity due to the rotation of nanofilm, indicating the anisotropic interference effect of the quasi-2D nanofilm, which confirms that the helical Te atom chains are oriented along the growth direction and match the TEM results (Figure 5d). Besides, due to the coalescence between two adjacent NWs, the crystal structure changed to form a microscale 2D material, which alters the electrical transport property. Moreover, electric conductivity was also improved as the gap between NWs disappeared (Supplementary Figure 14).

CONCLUSION

In summary, we have developed an IAIS strategy for preparing centimeter-scale quasi-2D Te nanofilms with good crystallinity and considerable anisotropic transport properties. The formation process mainly contains the crystal plane orientation and the oriented attachment between Te NWs. For the crystal-plane-oriented process, the lowest ensemble-averaged interaction energy of 1D Te NWs on the liquid surface confirmed the configurations of the ordered crystal orientation. For the oriented attachment process, the molecular dynamics simulation demonstrates the behavior of the attached NWs with each other under an elevated temperature, driving the transformation from aligned 1D NWs into a quasi-2D Te nanofilm. In addition, the experimental results as well as the MC simulation prove the underlying mechanism of morphological changes during the attachment process. That is, Te atoms prefer to move from the sites on the convex boundary to sites on the concave boundary to obtain a smaller surface-to-volume ratio, leading to flattening of the nanofilm and diminishment of the nanopores. Identifying the pathways for the formation of these quasi-2D nanofilms involving 1D-to-2D transformations provides critical insights into the design and synthesis of 2D materials.

ASSOCIATED CONTENT

Supporting Information

The Supporting Information is available free of charge at https://pubs.acs.org/doi/10.1021/jacs.4c03730.

Supplementary notes on dynamics simulation and Monte Carlo simulations of atom rearrangement; structural characterizations (PDF)

Video S1 (MP4)

Video S2 (MP4)

Video S3 (MP4)

Video S4 (MP4)

Video S5 (MP4)

AUTHOR INFORMATION

Corresponding Authors

Zhen He − *Shenzhen Key Laboratory of Sustainable Biomimetic Materials, Department of Materials Science and Engineering, Institute of Innovative Materials, Southern University of Science and Technology Guangming Advanced Research Institute, Southern University of Science and Technology, Shenzhen 518055, China; New Cornerstone Science Laboratory, Division of Nanomaterials & Chemistry, Hefei National Research Center for Physical Sciences at the Microscale, Department of Chemistry, Institute of Biomimetic Materials & Chemistry, Anhui Engineering Laboratory of Biomimetic Materials, University of Science and Technology of China, Hefei 230026, China*; Email: hez@sustech.edu.cn

Hui-Jun Jiang − *Hefei National Research Center for Physical Sciences at the Microscale, Department of Chemical Physics, iChEM, University of Science and Technology of China, Hefei*

https://doi.org/10.1021/jacs.4c03730
J. Am. Chem. Soc. 2024, 146, 19998−20008

*230026, China; orcid.org/0000-0001-7243-5431; Email: hjjiang3@ustc.edu.cn

Jian-Wei Liu − *New Cornerstone Science Laboratory, Division of Nanomaterials & Chemistry, Hefei National Research Center for Physical Sciences at the Microscale, Department of Chemistry, Institute of Biomimetic Materials & Chemistry, Anhui Engineering Laboratory of Biomimetic Materials, University of Science and Technology of China, Hefei 230026, China;* orcid.org/0000-0001-9237-1025; Email: jwliu13@ustc.edu.cn

Shu-Hong Yu − *Shenzhen Key Laboratory of Sustainable Biomimetic Materials, Department of Materials Science and Engineering, Institute of Innovative Materials, Southern University of Science and Technology Guangming Advanced Research Institute, Southern University of Science and Technology, Shenzhen 518055, China; New Cornerstone Science Laboratory, Division of Nanomaterials & Chemistry, Hefei National Research Center for Physical Sciences at the Microscale, Department of Chemistry, Institute of Biomimetic Materials & Chemistry, Anhui Engineering Laboratory of Biomimetic Materials, University of Science and Technology of China, Hefei 230026, China;* orcid.org/0000-0003-3732-1011; Email: shyu@ustc.edu.cn

Authors

Jie Su − *Hefei National Research Center for Physical Sciences at the Microscale, Department of Chemical Physics, iChEM, University of Science and Technology of China, Hefei 230026, China*

Yu-Tao Wang − *Shenzhen Key Laboratory of Sustainable Biomimetic Materials, Department of Materials Science and Engineering, Institute of Innovative Materials, Southern University of Science and Technology Guangming Advanced Research Institute, Southern University of Science and Technology, Shenzhen 518055, China*

Kang Wang − *New Cornerstone Science Laboratory, Division of Nanomaterials & Chemistry, Hefei National Research Center for Physical Sciences at the Microscale, Department of Chemistry, Institute of Biomimetic Materials & Chemistry, Anhui Engineering Laboratory of Biomimetic Materials, University of Science and Technology of China, Hefei 230026, China*

Jin-Long Wang − *Shenzhen Key Laboratory of Sustainable Biomimetic Materials, Department of Materials Science and Engineering, Institute of Innovative Materials, Southern University of Science and Technology Guangming Advanced Research Institute, Southern University of Science and Technology, Shenzhen 518055, China*

Yi Li − *New Cornerstone Science Laboratory, Division of Nanomaterials & Chemistry, Hefei National Research Center for Physical Sciences at the Microscale, Department of Chemistry, Institute of Biomimetic Materials & Chemistry, Anhui Engineering Laboratory of Biomimetic Materials, University of Science and Technology of China, Hefei 230026, China*

Rui Wang − *New Cornerstone Science Laboratory, Division of Nanomaterials & Chemistry, Hefei National Research Center for Physical Sciences at the Microscale, Department of Chemistry, Institute of Biomimetic Materials & Chemistry, Anhui Engineering Laboratory of Biomimetic Materials, University of Science and Technology of China, Hefei 230026, China*

Qing-Xia Chen − *New Cornerstone Science Laboratory, Division of Nanomaterials & Chemistry, Hefei National Research Center for Physical Sciences at the Microscale, Department of Chemistry, Institute of Biomimetic Materials & Chemistry, Anhui Engineering Laboratory of Biomimetic Materials, University of Science and Technology of China, Hefei 230026, China*

Zhong-Huai Hou − *Hefei National Research Center for Physical Sciences at the Microscale, Department of Chemical Physics, iChEM, University of Science and Technology of China, Hefei 230026, China;* orcid.org/0000-0003-1241-7041

Complete contact information is available at: https://pubs.acs.org/10.1021/jacs.4c03730

Author Contributions

†Z.H. and J.S. contributed equally.

Notes

The authors declare no competing financial interest.

■ ACKNOWLEDGMENTS

This work was supported by the National Natural Science Foundation of China (22005287, 22375083, 22175164, 22293044, 22005289, 92263102, 22373090), the Shenzhen Science and Technology Program (ZDSYS20220401161800001), High Level of Special Funds (G03050K002), the National Key Research and Development Program of China (2021YFA0715700, 2018YFE0202201), the Major Basic Research Project of Anhui Province (2023z04020009), the USTC Research Funds of the Double First-Class Initiative (YD9990002019), and the New Cornerstone Science Foundation. This work was partially carried out at the USTC Center for Micro and Nanoscale Research and Fabrication. The authors thank beamline BL16B1 (Shanghai Synchrotron Radiation Faculty) for providing the beam time, Prof. Hao-Liang Huang from SUSTech for providing the in-plane XRD measure mapping, and Prof. Jin-Hui Zhong and Mr. Kai-Zhen Liu for providing the angle-resolved Raman spectrum testing.

■ REFERENCES

(1) Wang, H.-P.; Li, S.; Liu, X.; Shi, Z.; Fang, X.; He, J.-H. Low-Dimensional Metal Halide Perovskite Photodetectors. *Adv. Mater.* **2021**, *33* (7), No. 2003309.

(2) Garnett, E.; Mai, L.; Yang, P. Introduction: 1D Nanomaterials/Nanowires. *Chem. Rev.* **2019**, *119* (15), 8955−8957.

(3) Xia, Y.; Chen, Q.; Banin, U. Introduction: Anisotropic Nanomaterials. *Chem. Rev.* **2023**, *123* (7), 3325−3328.

(4) Guan, Y.; Zhang, C.; Liu, Z.; Zhao, Y.; Ren, A.; Liang, J.; Hu, F.; Zhao, Y. S. Single-Crystalline Perovskite p−n Junction Nanowire Arrays for Ultrasensitive Photodetection. *Adv. Mater.* **2022**, *34* (35), No. 2203201.

(5) Li, M.; Lu, H.-W.; Wang, S.-W.; Li, R.-P.; Chen, J.-Y.; Chuang, W.-S.; Yang, F.-S.; Lin, Y.-F.; Chen, C.-Y.; Lai, Y.-C. Filling the gap between topological insulator nanomaterials and triboelectric nanogenerators. *Nat. Commun.* **2022**, *13* (1), 938.

(6) Teitsworth, T. S.; Hill, D. J.; Litvin, S. R.; Ritchie, E. T.; Park, J.-S.; Custer, J. P.; Taggart, A. D.; Bottum, S. R.; Morley, S. E.; Kim, S.; McBride, J. R.; Atkin, J. M.; Cahoon, J. F. Water splitting with silicon p-i-n superlattices suspended in solution. *Nature* **2023**, *614* (7947), 270−274.

(7) Zhou, B.; Ma, Y.; Ou, P.; Ye, Z.; Li, X.-Y.; Vanka, S.; Ma, T.; Sun, H.; Wang, P.; Zhou, P.; Cooper, J. K.; Xiao, Y.; Navid, I. A.; Pan, J.; Song, J.; Mi, Z. Light-driven synthesis of C_2H_6 from CO_2 and H_2O

on a bimetallic AuIr composite supported on InGaN nanowires. *Nat. Catal.* **2023**, *6* (11), 987−995.
(8) Li, H.; Teal, D.; Liang, Z.; Kwon, H.; Huo, D.; Jin, A.; Fischer, P.; Fan, D. E. Precise electrokinetic position and three-dimensional orientation control of a nanowire bioprobe in solution. *Nat. Nanotechnol.* **2023**, *18* (10), 1213−1221.
(9) Guo, P.; Tian, B.; Liang, J.; Yang, X.; Tang, G.; Li, Q.; Liu, Q.; Zheng, K.; Chen, X.; Wu, W. An All-Printed, Fast-Response Flexible Humidity Sensor Based on Hexagonal-WO_3 Nanowires for Multifunctional Applications. *Adv. Mater.* **2023**, *35* (41), No. 2304420.
(10) Kim, T. Y.; Hong, S. H.; Jeong, S. H.; Bae, H.; Cheong, S.; Choi, H.; Hahn, S. K. Multifunctional Intelligent Wearable Devices Using Logical Circuits of Monolithic Gold Nanowires. *Adv. Mater.* **2023**, *35* (45), No. 2303401.
(11) Loeffler, A.; Diaz-Alvarez, A.; Zhu, R.; Ganesh, N.; Shine, J. M.; Nakayama, T.; Kuncic, Z. Neuromorphic learning, working memory, and metaplasticity in nanowire networks. *Sci. Adv.* **2023**, *9*, No. eadg3289.
(12) Guo, S.; Tan, J.; Zhang, H.; Wang, J.; Ji, T.; Zhang, L.; Hu, X.; Chen, J.; Xie, J.; Zou, K.; Meng, Y.; Bei, X.; Wu, L.-A.; Chen, Q.; Wang, H.; Tu, X.; Jia, X.; Zhao, Q.-Y.; Kang, L.; Wu, P. High-timing-precision detection of single X-ray photons by superconducting nanowires. *Natl. Sci. Rev.* **2023**, *11*, No. nwad102.
(13) Guo, X.; Wu, D.; Li, Y.; He, Z.; Wang, J.-L.; Zhang, C.; Pan, Z.; Pang, Y.; Zhuang, T.; Yu, S.-H. Ordering silver nanowires for chiroptical activity. *Sci. China Mater.* **2022**, *65* (5), 1362−1368.
(14) Zeng, G.; Chen, W.; Chen, X.; Hu, Y.; Chen, Y.; Zhang, B.; Chen, H.; Sun, W.; Shen, Y.; Li, Y.; Yan, F.; Li, Y. Realizing 17.5% Efficiency Flexible Organic Solar Cells via Atomic-Level Chemical Welding of Silver Nanowire Electrodes. *J. Am. Chem. Soc.* **2022**, *144* (19), 8658−8668.
(15) Chen, J.; Bai, Y.; Feng, J.; Yang, F.; Xu, P.; Wang, Z.; Zhang, Q.; Yin, Y. Anisotropic Seeded Growth of Ag Nanoplates Confined in Shape-Deformable Spaces. *Angew. Chem., Int. Ed.* **2021**, *60* (8), 4117−4124.
(16) Qin, J.-K.; Liao, P.-Y.; Si, M.; Gao, S.; Qiu, G.; Jian, J.; Wang, Q.; Zhang, S.-Q.; Huang, S.; Charnas, A.; Wang, Y.; Kim, M. J.; Wu, W.; Xu, X.; Wang, H.-Y.; Yang, L.; Khin Yap, Y.; Ye, P. D. Raman response and transport properties of tellurium atomic chains encapsulated in nanotubes. *Nat. Electron.* **2020**, *3* (3), 141−147.
(17) Calavalle, F.; Suárez-Rodríguez, M.; Martín-García, B.; Johansson, A.; Vaz, D. C.; Yang, H.; Maznichenko, I. V.; Ostanin, S.; Mateo-Alonso, A.; Chuvilin, A.; Mertig, I.; Gobbi, M.; Casanova, F.; Hueso, L. E. Gate-tuneable and chirality-dependent charge-to-spin conversion in tellurium nanowires. *Nat. Mater.* **2022**, *21* (5), 526−532.
(18) Wang, R.; Wang, J.-L.; Liu, T.; He, Z.; Wang, H.; Liu, J.-W.; Yu, S.-H. Controllable Inverse Photoconductance in Semiconducting Nanowire Films. *Adv. Mater.* **2022**, *34* (36), No. 2204698.
(19) Zhang, N.; Zhao, G.; Li, L.; Wang, P.; Xie, L.; Cheng, B.; Li, H.; Lin, Z.; Xi, C.; Ke, J.; Yang, M.; He, J.; Sun, Z.; Wang, Z.; Zhang, Z.; Zeng, C. Magnetotransport signatures of Weyl physics and discrete scale invariance in the elemental semiconductor tellurium. *Proc. Natl. Acad. Sci. U. S. A.* **2020**, *117* (21), 11337−11343.
(20) Zhao, C.; Batiz, H.; Yasar, B.; Kim, H.; Ji, W.; Scott, M. C.; Chrzan, D. C.; Javey, A. Tellurium Single-Crystal Arrays by Low-Temperature Evaporation and Crystallization. *Adv. Mater.* **2021**, *33* (37), No. 2100860.
(21) Lu, J.; He, Y.; Ma, C.; Ye, Q.; Yi, H.; Zheng, Z.; Yao, J.; Yang, G. Ultrabroadband Imaging Based on Wafer-Scale Tellurene. *Adv. Mater.* **2023**, *35* (20), No. 2211562.
(22) Fu, H.; Xu, Y.; Qiu, D.; Ma, T.; Yue, G.; Zeng, Z.; Song, L.; Wang, S.; Zhang, S.; Du, Y.; Yan, C.-H. A Library of Rare Earth Oxide Ultrathin Nanowires with Polymer-Like Behaviors. *Angew. Chem., Int. Ed.* **2022**, *61* (45), No. e202212251.
(23) Tang, Z.; Kotov, N. A.; Giersig, M. Spontaneous Organization of Single CdTe Nanoparticles into Luminescent Nanowires. *Science* **2002**, *297* (5579), 237−240.
(24) Liu, Q.; He, S.; Yu, B.; Cheng, X.; Shi, W.; Wang, X. Visible Light Induced Ag−Polyoxometalate Coassembly into Single-Cluster Nanowires. *Adv. Mater.* **2022**, *34* (40), No. 2206178.
(25) Pan, J.; Li, X.; Gong, X.; Yin, J.; Zhou, D.; Sinatra, L.; Huang, R.; Liu, J.; Chen, J.; Dursun, I.; El-Zohry, A. M.; Saidaminov, M.; Sun, H.-T.; Mohammed, O. F.; Ye, C.; Sargent, E. H.; Bakr, O. Halogen Vacancies Enable Ligand-Assisted Self-assembly of Perovskite Quantum Dots into Nanowires. *Angew. Chem., Int. Ed.* **2019**, *58* (45), 16077−16081.
(26) Li, Z.-J.; Hofman, E.; Davis, A. H.; Maye, M. M.; Zheng, W. General Strategy for the Growth of $CsPbX_3$ (X = Cl, Br, I) Perovskite Nanosheets from the Assembly of Nanorods. *Chem. Mater.* **2018**, *30* (11), 3854−3860.
(27) Yang, J.; Zeng, Z.; Kang, J.; Betzler, S.; Czarnik, C.; Zhang, X.; Ophus, C.; Yu, C.; Bustillo, K.; Pan, M.; Qiu, J.; Wang, L.-W.; Zheng, H. Formation of two-dimensional transition metal oxide nanosheets with nanoparticles as intermediates. *Nat. Mater.* **2019**, *18* (9), 970−976.
(28) Bomal, E.; Grandgeorge, P.; Yeo, R. J.; Candau, N.; Reis, P. M.; Frauenrath, H. Spontaneous formation of a self-healing carbon nanoskin at the liquid-liquid interface. *Nat. Commun.* **2022**, *13* (1), 4950.
(29) Seki, T.; Yu, X.; Zhang, P.; Yu, C.-C.; Liu, K.; Gunkel, L.; Dong, R.; Nagata, Y.; Feng, X.; Bonn, M. Real-time study of on-water chemistry: Surfactant monolayer-assisted growth of a crystalline quasi-2D polymer. *Chem* **2021**, *7* (10), 2758−2770.
(30) Zhong, Y.; Cheng, B.; Park, C.; Ray, A.; Brown, S.; Mujid, F.; Lee, J.-U.; Zhou, H.; Suh, J.; Lee, K.-H.; Mannix, A. J.; Kang, K.; Sibener, S. J.; Muller, D. A.; Park, J. Wafer-scale synthesis of monolayer two-dimensional porphyrin polymers for hybrid superlattices. *Science* **2019**, *366* (6471), 1379−1384.
(31) Chen, C.; Zhao, B.; Wang, R.; He, Z.; Wang, J. L.; Hu, M.; Li, X. L.; Pei, G.; Liu, J. W.; Yu, S. H. Janus Helical Ribbon Structure of Ordered Nanowire Films for Flexible Solar Thermoelectric Devices. *Adv. Mater.* **2022**, *34* (44), No. 2206364.
(32) Tao, A.; Kim, F.; Hess, C.; Goldberger, J.; He, R.; Sun, Y.; Xia, Y.; Yang, P. Langmuir-Blodgett Silver Nanowire Monolayers for Molecular Sensing Using Surface-Enhanced Raman Spectroscopy. *Nano Lett.* **2003**, *3* (9), 1229−1233.
(33) Yang, P.; Kim, F. Langmuir-Blodgett Assembly of One-Dimensional Nanostructures. *ChemPhysChem* **2002**, *3* (6), 503−506.
(34) Kim, F.; Kwan, S.; Akana, J.; Yang, P. Langmuir-Blodgett Nanorod Assembly. *J. Am. Chem. Soc.* **2001**, *123* (18), 4360−4361.
(35) Tao, A. R.; Huang, J.; Yang, P. Langmuir-Blodgettry of Nanocrystals and Nanowires. *Acc. Chem. Res.* **2008**, *41* (12), 1662−1673.
(36) Acharya, S.; Hill, J. P.; Ariga, K. Soft Langmuir-Blodgett Technique for Hard Nanomaterials. *Adv. Mater.* **2009**, *21* (29), 2959−2981.
(37) Linares-Moreau, M.; Brandner, L. A.; Velásquez-Hernández, M. d. J.; Fonseca, J.; Benseghir, Y.; Chin, J. M.; Maspoch, D.; Doonan, C.; Falcaro, P. Fabrication of Oriented Polycrystalline MOF Superstructures. *Adv. Mater.* **2024**, *36* (1), No. 2309645.
(38) Kuang, H.; Chen, L.; Hao, C.; Cai, J.; Chen, C.; Ma, W.; Xu, C.; Xu, L. Chiral Self-Assembled Film from Semiconductor Nanorods with Ultra-strong Circularly Polarized Luminescence. *Angew. Chem., Int. Ed.* **2021**, *60* (50), 26276−26280.
(39) Deng, K.; Luo, Z.; Tan, L.; Quan, Z. Self-assembly of anisotropic nanoparticles into functional superstructures. *Chem. Soc. Rev.* **2020**, *49* (16), 6002−6038.
(40) Linares-Moreau, M.; Brandner, L. A.; Kamencek, T.; Klokic, S.; Carraro, F.; Okada, K.; Takahashi, M.; Zojer, E.; Doonan, C. J.; Falcaro, P. Semi-Automatic Deposition of Oriented $Cu(OH)_2$ Nanobelts for the Heteroepitaxial Growth of Metal-Organic Framework Films. *Adv. Mater. Interfaces* **2021**, *8* (21), No. 2101039.
(41) Londoño-Calderon, A.; Williams, D. J.; Ophus, C.; Pettes, M. T. 1D to 2D Transition in Tellurium Observed by 4D Electron Microscopy. *Small* **2020**, *16* (49), No. 2005447.

https://doi.org/10.1021/jacs.4c03730
J. Am. Chem. Soc. 2024, 146, 19998−20008

(42) Liu, J.-W.; Zhu, J.-H.; Zhang, C.-L.; Liang, H.-W.; Yu, S.-H. Mesostructured assemblies of ultrathin superlong tellurium nanowires and their photoconductivity. *J. Am. Chem. Soc.* **2010**, *132* (26), 8945−8952.
(43) Alshareedah, I.; Moosa, M. M.; Raju, M.; Potoyan, D. A.; Banerjee, P. R. Phase transition of RNA-protein complexes into ordered hollow condensates. *Proc. Natl. Acad. Sci. U. S. A.* **2020**, *117* (27), 15650−15658.
(44) He, Z.; Jiang, H. J.; Wu, L. L.; Liu, J. W.; Wang, G.; Wang, X.; Wang, J. L.; Hou, Z. H.; Chen, G.; Yu, S. H. Real-Time Probing of Nanowire Assembly Kinetics at the Air-Water Interface by In Situ Synchrotron X-Ray Scattering. *Angew. Chem., Int. Ed.* **2018**, *57* (27), 8130−8134.
(45) Ben-Moshe, A.; da Silva, A.; Müller, A.; Abu-Odeh, A.; Harrison, P.; Waelder, J.; Niroui, F.; Ophus, C.; Minor, A. M.; Asta, M.; Theis, W.; Ercius, P.; Alivisatos, A. P. The chain of chirality transfer in tellurium nanocrystals. *Science* **2021**, *372* (6543), 729−733.
(46) Ge, Y.; Duan, X.; Zhang, M.; Mei, L.; Hu, J.; Hu, W.; Duan, X. Direct Room Temperature Welding and Chemical Protection of Silver Nanowire Thin Films for High Performance Transparent Conductors. *J. Am. Chem. Soc.* **2018**, *140* (1), 193−199.
(47) Wang, F.; Sun, W.; Gao, Y.; Liu, Y.; Zhao, J.; Sun, C. Investigation on the most probable breaking behaviors of copper nanowires with the dependence of temperature. *Comput. Mater. Sci.* **2013**, *67*, 182−187.
(48) Sankaranarayanan, S. K. R. S.; Bhethanabotla, V. R.; Joseph, B. Molecular dynamics simulation of temperature and strain rate effects on the elastic properties of bimetallic Pd-Pt nanowires. *Phys. Rev. B* **2007**, *76* (13), No. 134117.
(49) Zhao, C.; Tan, C.; Lien, D. H.; Song, X.; Amani, M.; Hettick, M.; Nyein, H. Y. Y.; Yuan, Z.; Li, L.; Scott, M. C.; Javey, A. Evaporated tellurium thin films for p-type field-effect transistors and circuits. *Nat. Nanotechnol.* **2020**, *15* (1), 53−58.
(50) Wang, Y.; Qiu, G.; Wang, R.; Huang, S.; Wang, Q.; Liu, Y.; Du, Y.; Goddard, W. A.; Kim, M. J.; Xu, X.; Ye, P. D.; Wu, W. Field-effect transistors made from solution-grown two-dimensional tellurene. *Nat. Electron.* **2018**, *1* (4), 228−236.
(51) Pine, A. S.; Dresselhaus, G. F. Raman Spectra and Lattice Dynamics of Tellurium. *Phys. Rev. B* **1971**, *4*, 356−371.

https://doi.org/10.1021/jacs.4c03730
J. Am. Chem. Soc. 2024, 146, 19998−20008